

A Programmably Compliant Origami Mechanism for Dynamically Dexterous Robots

Wei-Hsi Chen, Shivangi Misra, Yuchong Gao, Young-Joo Lee,
Daniel E. Koditschek, Shu Yang, Cynthia R. Sung

Abstract—We present an approach to overcoming challenges in dynamical dexterity for robots through programmably compliant origami mechanisms. Our work leverages a one-parameter family of flat sheet crease patterns that folds into origami bellows, whose axial compliance can be tuned to select desired stiffness. Concentrically arranged cylinder pairs reliably manifest additive stiffness, extending the programmable range by nearly an order of magnitude and achieving bulk axial stiffness spanning 200–1500 N m⁻¹ using 8 mil thick polyester-coated paper. Accordingly, we design origami energy-storing springs with a stiffness of 1035 N m⁻¹ each and incorporate them into a three degree-of-freedom (DOF) tendon-driven spatial pointing mechanism that exhibits trajectory tracking accuracy less than 15% rms error within a (~ 2 cm)³ volume. The origami springs can sustain high power throughput, enabling the robot to achieve asymptotically stable juggling for both highly elastic (1 kg resilient shotput ball) and highly damped (“medicine ball”) collisions in the vertical direction with apex heights approaching 10 cm. The results demonstrate that “soft” robotic mechanisms are able to perform a controlled, dynamically actuated task.

Index Terms—Soft Robot Applications; Soft Robot Materials and Design; Compliant Joint/Mechanism

I. INTRODUCTION

OVER decades of robot manipulation [1] and locomotion [2] research, the term *dynamical dexterity* has come to mean the programmed [3] exchange of work and information at high temporal rates [4]. Indeed, sensorimotor dexterity [5] is essential to the quality of our daily life [6], specifically in the high-strength regime [7]. As robots begin to enter the unstructured workplace, their users’ expectation of companionable dexterity will continue to sharpen the intrinsic conflict between the need for more actuated degrees of freedom and the requirement of high power density [8], whose limits in the relevant highly energetic and high strength regime have long manifested as the first scarce resource in conventional robot actuation technologies [9].

Manuscript received: September 10, 2019; Revised December 12, 2019; Accepted January 9, 2020. This paper was recommended for publication by Editor Kyu-Jin Cho upon evaluation of the Associate Editor and Reviewers’ comments. This work is supported in part by the Army Research Office (ARO) under the SLICE Multidisciplinary University Research Initiatives (MURI) Program, award #W911NF1810327 and the National Science Foundation (NSF) grant #1845339. We thank J. Diego Caporale for technical consultant and Diedra Krieger for administrative support.

W.-H. Chen, S. Misra, Y. Gao, Y.-J. Lee, D. E. Koditschek, S. Yang, C. R. Sung are with the General Robotics, Autonomous, Sensing and Perception (GRASP) Lab, University of Pennsylvania, Philadelphia, Philadelphia 19104, United States (e-mail: {weicc, shivangi, yuchongg, yjoolee, kod, shuyang, crsung}@seas.upenn.edu)

Digital Object Identifier (DOI): see top of this page.

The use of soft materials of varied shape and programmable compliance enjoys an active literature in contemporary robotics [10] and beyond [11] as a method for introducing both high maneuverability and resilience directly into the body of a robot. However, while compliant elastomeric robots have occasionally been demonstrated to produce fast, dynamic [12], and even explosive [13] maneuvers, the high damping and high fatigue properties in these elastomers often limit these maneuvers to a single use. Meanwhile, sustained dynamic motions needed for tasks such as juggling, hopping, and trotting, remain out of reach for most soft robots.

Origami-inspired approaches to replacing [14] or enhancing [15] soft-bodied machines promise to address these challenges in achieving repeated, dynamic movement. Mechanisms built with origami structures take their place within the “soft” robotics literature by virtue of the high degree of freedom, very low stiffness properties of their constituent thin sheets, while benefiting from the insights of the metamaterials literature to program their bulk properties through carefully designed anisotropic arrangements of their constituent parts. Past research in this field has demonstrated durable actuators from origami cylinders, yielding lightweight structures [16], [17], [18], [19] patterned by high compliance folds. The resulting actuators assert high specific force [20] over a large volume-to-mass workspace [21], and bear substantial loads [15] while resisting unwanted (e.g., torsional) disturbances [22]. However, to date, origami robots have been designed as though with rigid linkages joined through rotational folds, without taking into consideration of the additional compliance and resiliency provided by the sheet material itself. As a result, they have been unable to match the *power* densities of the rigid-body counterparts.

In this paper, we explore the prospects for integrating programmable [23], [24] compliance and highly energetic anisotropic designs in the drivetrain of a three DOF robotic limb through the lens of the vertical one-juggle [1], a well-established route toward dynamically dexterous manipulation and locomotion [25]. With this targeted locomotion application in view, our ability to program the effective bulk stiffness at design time over an order of magnitude offers the promise of building running machines at a comparable range of mass scales from the very same materials, and essentially the same design. Through geometric designs of an origami bellow pattern [26], we aim to achieve elastic axial compliance with reduced material weight and mitigation of energetic loss, thus producing a “soft” spring robotic juggler capable of high-power operation. The resistance of an origami design to static

loading conditions can be tuned through appropriate selection of the material properties in the folds [27], [28], or, as an important contrast, without any variation in the base material, through the pattern expressed in its geometric parameters, as suggested in origami mechanics literature [29], [30]. Here, we demonstrate that the *dynamic* response of an origami pattern can also be tuned, and that the resulting structure is in fact capable of transducing the high power densities required for dynamical dexterity.

Specifically, we leverage the Reconfigurable Expanding Bistable Origami (REBO) pattern [26], which was originally designed for geometric reconfiguration. Interestingly, we find that small changes in the fold pattern alter not only the geometry of the structure, but also its rigidity. Thus, we manipulate the REBO design parameters for a dynamic juggling task and introduce a concentric pairing of the REBO cylinders to enhance stiffness. We drive three such concentrically paired cylinders to achieve $3 \times 10^3 \text{ N m}^{-1}$ stiffness and compress each via a conventionally actuated tendon. The resulting three-DOF “limb” achieves reasonably good trajectory tracking (less than 15% rms error) within a workspace whose actuated volume is limited to a small fraction of its kinematically achievable span by the torque output of the brushless DC motors. Nevertheless, this volume affords adequate travel and the paired REBO cylinders transduce sufficiently high power to achieve asymptotically stable vertical juggling of balls of varied mass and resilience.

In summary, the contribution of this work is the development, analysis, and application of a new approach for dynamically dexterous manipulation; it substitutes an origami structure for a conventional spring, storing sufficient energy and transducing it with sufficient power and force to juggle stably a 1 kg mass to a height selectable over a range of nearly 10 cm, from initial conditions within a similarly large basin of attraction.

II. ORIGAMI MODULE DESIGN

A. Parameterized Programmable Crease Pattern

The REBO design (Fig. 1(a)) is an origami bellows. The fold pattern is a tessellation of rectangular units arranged into n_r columns and n_l rows, with the left and right columns glued together to form a tube. Each unit contains a middle crease at an angle α from horizontal, as shown in the grey box in Fig. 1(a). When folded, these creases cause each row of the structure to collapse into a n_r -sided right frustum with height $\frac{1}{2}\Delta z$ and side lengths $(a_o - b_o)$ and $(a_i - b_i)$ on the larger and smaller bases (Fig. 1(b)). We define the angle between the base and side of the layer as the cone angle β .

There is a direct relationship between the geometric parameters of the fold pattern and those of the 3-D folded state. In particular, the rotation angle θ of each trapezoid shown in Fig. 1(b) is $\theta = (2\pi \cos \beta)/n_r$. The values of α and h can then be calculated as $\alpha = (\pi - \theta)/2$ and $h = (\Delta z \csc \beta)/2$.

The design has the ability to store potential energy in the bending of the folds and the stretching of the faces, similarly to the multistable “bendy straw” design [31]. Interestingly, by changing the size of the design and geometric parameters such

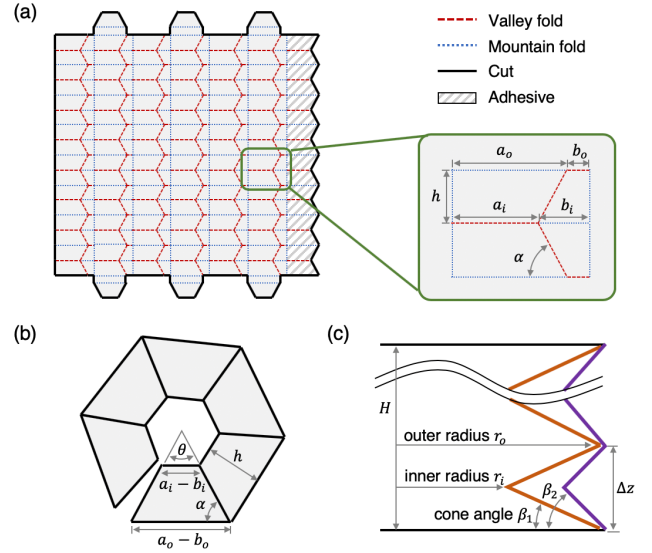


Fig. 1. Origami REBO design (a) the crease pattern of REBO (b) schematic diagram of one layer of REBO when folded flat (c) schematic diagram of the cross section of the right half of the the double layer REBO structure, where the purple and orange line indicates different layers. β denotes the cone angle, where the index indicates the different layer

as β and Δz , the amount of structural deformation required for the design to bend and compress can be manipulated, thus allowing us to control the stiffness of the design purely through its geometry. When β is 0, the folded state is a flat polygon with little resistance to axial forces. This is because the flat folded configuration relies on torsional stiffness in the folds, which is typically small. As β increases, the slope of each layer increases, and REBO cannot be folded flat without deformation of the sheet surfaces. In other words, the potential energy of compressing the structure is now stored not only in the folds, but also in the surfaces, making the structure stiffer. Thus by designing β , one can generate spring-like structures with variable degree of stiffness.

B. Effect of Cone Angle on Stiffness

To understand the relation between the cone angle and the stiffness of the REBO, we folded multiple versions of the pattern with variable geometric parameters and conducted compression tests. The parameters chosen for this study were as follows: $a_o = 20 \text{ mm}$, $b_o = 6 \text{ mm}$, $\Delta z = 10 \text{ mm}$, $n_r = 6$, and a total of $n_l = 8$ layers. We tested cone angles β between 15° and 45° , with increments of 5° in between. The crease patterns are generated from a MATLAB script. The patterns’ outlines are cut out and the folds perforated using a laser cutter, and then the sheet is manually folded for each bellows. The process takes about 30 minutes. All samples discussed in this paper are folded using 8 mil thick Durilla synthetics paper with polyester finish (CTI Paper, USA) and their seams are sealed using 3M 467MP adhesive transfer tape to glue the left and right sides together as a closed cylinder. Fig. 2(a) shows the results of the fabrication. The theoretical rest length of all of these REBO structures should be $l_t = n_l \Delta z = 80 \text{ mm}$. However, due to the imperfection of manual folding, the final rest lengths are not equal, and in fact decrease as β increases.

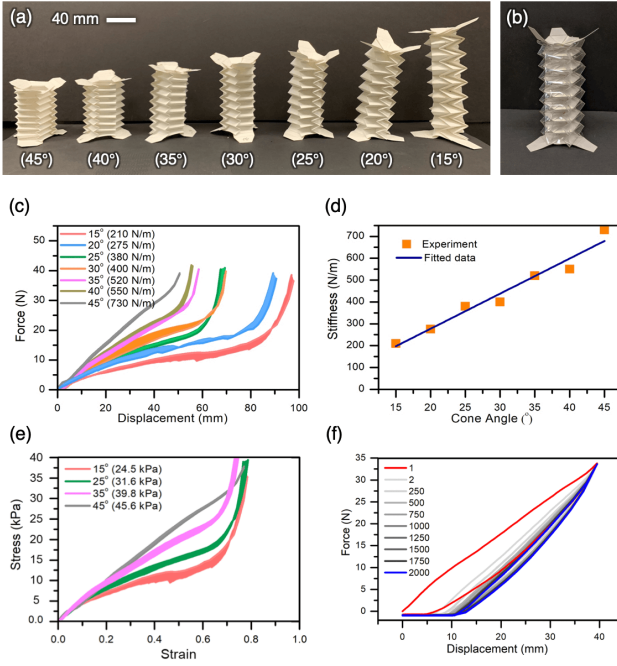


Fig. 2. Material performance, compressive stiffness vs. cone angle: (a) specimens of different cone angles, (b) the double layer REBO structure with a transparent outer layer and a white inner layer, (c) compressive force vs. displacement, (d) linear fit of the stiffness experiments, (e) compressive stress vs. strain, (f) cyclic test.

The true rest lengths l_{real} were measured and used for the following experiments.

We used an Instron Model 5564 with 100N compression load cell to measure the force required to compress each specimen from its natural length l_{real} until all the layers were stacked flat and the force exceeded 40N. Each specimen was measured 5 times.

The result of the experiment is shown in Fig. 2(c). The shaded regions show the minimum and maximum force values corresponding to each displacement for the sample. The results show that REBO structure exhibits a Hookean force-displacement curve for well over 2/3 of its total travel. We computed the effective stiffness (elastic constant) as the slope of the linear fit in this region. The sharp increase in stiffness at the end of the curve corresponds to all of the layers coming into contact with each other so that the specimen can be viewed as a solid cylinder. This region should be avoided during application. Fig. 2(d) summarizes the mean effective stiffness for each of the measured samples. A linear fit indicates that the stiffness K_s increases as a roughly affine function of the cone angle β , $K_s = 16.06\beta - 43.71$, with $R^2 = 0.95$. The REBO design was able to achieve a broad range of stiffnesses from 210 N m^{-1} to 730 N m^{-1} . The stiffer the compliance we require, the less base material mass we need; as β increases, h decreases, hence more paper is used to produce the deeper cone angle of a less stiff REBO spring. In sharp contrast, the stiffness of traditional springs is intrinsic to their bulk material capacity to resist elastic deformation. Thus, more material mass will be needed to achieve greater stiffness. Clearly, the REBO metamaterial provides a promising alternative that can transduce greater

TABLE I
STIFFNESS OF DOUBLE-LAYERED REBO

Inner layer (β_{il})	Outer layer (β_{ol})	Double layer
320 N m^{-1} (25°)	540 N m^{-1} (35°)	888 N m^{-1}
320 N m^{-1} (25°)	725 N m^{-1} (45°)	1035 N m^{-1}
700 N m^{-1} (35°)	725 N m^{-1} (45°)	1490 N m^{-1}

mass specific power than a conventional spring.

We computed stress-strain curves for the specimens (Fig. 2(e)). Strain was calculated using the real rest length l_{real} and stress using the compression force acting on the effective hexagonal area $A = 3\sqrt{3}(a_o - b_o)^2$, with the Young's modulus as the slope of the resulting curve. The results show that the cone angle does indeed have a significant effect beyond simply changing the length of REBO.

During experiments, we found that the dimensions of the REBO affect the stress-strain profile. For REBOs with the same cone angle β , a larger side length and height reduces the Young's modulus. As a result, a higher β is required to achieve a similar profile for a larger-scale model.

C. Double-Layered Design

The results show that a maximum stiffness of 730 N m^{-1} for the REBO design is achieved at $\beta = 45^\circ$. Above this β value, the structure is at risk of buckling irreversibly upon compression. However, higher stiffness can be achieved by arranging multiple REBO structures concentrically, as shown in Fig. 1(c) and 2(b). This parallel spring structure demonstrates additive stiffness and protects against snap-through buckling to the bistable inverted configurations, which were previously demonstrated in other applications [26], [32]. Here, three sets of double layer structure have been fabricated, with the cone angle of the inner and the outer structure to be $(25^\circ, 35^\circ)$, $(25^\circ, 45^\circ)$, and $(35^\circ, 45^\circ)$, respectively. To facilitate the fabrication of the double layered REBO structure, we increased b_o to make room for the inner structure to slide through, then refolded it to enclose it. A compression test was performed before and after the combination and the stiffness of each specimen was measured (see summary of results in Table I). The stiffness of springs arranged in parallel is theoretically additive since, for a given compression, the parallel springs simultaneously resist their individually supported loads. The experimental results show that the stiffness of the double layer structure is indeed the sum of the stiffnesses of the two individual layers with a maximum error of only 3.2%. We also observe that by increasing b_o , the stiffness decreases a little due to the fact that there is more space for the paper to deform.

D. Repeatability and Energy Loss

Finally, for dynamic robot applications, it is important to understand the energy dissipation and resilience of the REBO design. We therefore experimentally measured the response of a $\beta = 45^\circ$ REBO under cyclic loading. The specimen was alternately compressed and released between its original rest length and 40 mm displacement for 2000 cycles. Each cycle took 12 seconds. The results are shown in Fig. 2(f).

The Durilla synthetics paper used to fabricate the REBO structure in the present study is not ideally elastic. When the paper is initially folded, the crease regions generate highly localized strain. After initial loading surpassing the elastic deformation limit of the Durilla paper, the crease regions undergo permanent plastic deformation. Therefore, even after the compressive stress loaded in the whole REBO structure is released, mechanical offset strain due to the permanent deformation remains in the structure. As cyclic deformation proceeds, the polymer chains in the paper could disentangle, or even have chain scission, leading to further deformation at the creases, which eventually converges to a permanent bulk stress-strain relationship. The gradual and continuous shift of the stress-strain curve from the first cycle (red) to the final permanent curve (blue) is presented in Fig. 2(f). This behavior is consistent with literature in origami mechanics, where the first folding is often an outlier [33] since it plastically deforms the material and changes the structure's equilibrium state.

For repeated dynamic tasks, we are primarily concerned with the steady-state behaviors, i.e., the blue curve. We observed elastic hysteresis between the tension and compression portions of the tests, suggesting that more energy was required for loading comparing to unloading, and thermal energy was dissipated during this process. The displacement offset after 2000 runs is small compare to the original length, with a maximum of 3 mm, 5% of the rest length. After 2000 cycles, no physical damage was observed on the specimen and no failure was found on the force-displacement plot.

III. JUGGLING ROBOT DESIGN

Our characterization shows that stiffness on the order of 10^3 N m^{-1} , the range where energy exchange with 1 kg loads has been shown to achieve useful aerial-phase compliant-legged running gaits [34], can be easily accessible, and that this performance does not degrade over repeated uses. Armed with the understanding, we integrate the programmable compliance design to legged robots in the form of the “REBO Juggler.” Juggling a weighted ball continuously at a certain height requires a periodic motion and great power, similar to many dynamical locomotion tasks.

A. Robot Platform

The robot (Fig. 3) consists of four main parts: (a) the compliant REBO body, (b) force transmitting system composed of brushless DC electrical motor modules (Ghost Robotics MNSB01 Sub-Minitaur U8 Motor Module [35]) with tendon (Sufix 832 Advanced Superline Braid) and 3D-printed pulley system, (c) contact detection using force sensor (Ohmite FSR01CE), and (d) a microprocessor (Ghost Robotics MNS043 mainboard [35]) for integrating sensing and control. The compliant body, shown in Fig. 4(a), is composed by three double-layered REBO structures with a stiffness of 1035 N m^{-1} each. The parameters of the outer layer are $\beta = 45^\circ$, $a_o = 20 \text{ mm}$, $b_o = 5 \text{ mm}$, $\Delta z = 10 \text{ mm}$, $n_r = 6$, $n_l = 8$, and the ones for the inner layer are $\beta = 25^\circ$, $a_o = 19 \text{ mm}$, $b_o = 0 \text{ mm}$, $\Delta z = 10 \text{ mm}$, $n_r = 6$, $n_l = 8$. Each REBO weighs about 16 g. Three REBOs were

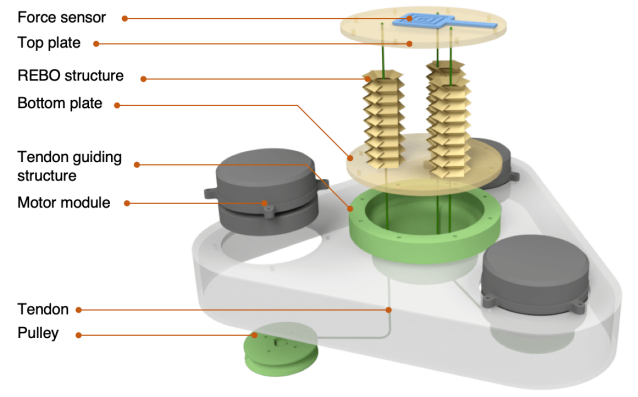


Fig. 3. CAD rendering of the REBO Juggler

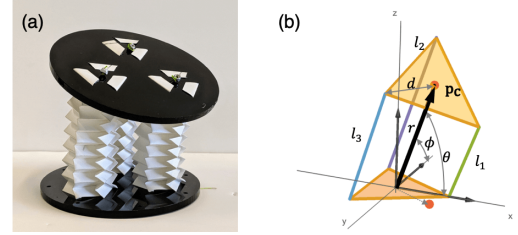


Fig. 4. (a) The compliant body composed of REBO. (b) Kinematic model of the REBO Juggler's tendon driven top plate under compressive load

then mounted between the top and bottom acrylic plates and secured using tabs, forming the compliant body that weighs about 220 g. The tendon was laced through the structural through-holes of REBO, with one end fixed on the top plate and the other on the pulley mounted on the motor. Rotating the motor compressed or released the REBO, and the speed limitation of the linear motion on REBO was determined by the motor. A force sensor was placed on top of the top plate to detect when an object was in contact with the top plate.

B. Kinematic Model

The robot platform can be modeled as two equilateral triangles connected at the corners by three tendons (Fig. 4(b)), where the change of tendon length changes the position and orientation of the top triangle. Let the origin of the model be at the center of the bottom triangle. The top and the bottom triangles have circumcircles of radius d . The linear actuator state is defined as $q_{la} = (l_1, l_2, l_3) \in [l_{min}, l_{max}]^3 = Q_{la}$, where l_1 , l_2 , and l_3 are the length of the three parallel linear actuators, and l_{min} , l_{max} are the length constraints of the actuators. The tendon is attached to a pulley mounted on the motor, where the motor state is defined as $q_m = (\theta_{m,1}, \theta_{m,2}, \theta_{m,3}) \in \mathbb{T}^3 = Q_m$, and the mapping from the motor space to the linear actuator space $q_{la} = f_1(q_m)$ is $l_i = l_0 + r_p \theta_{m,i}$, where the index i indicates different actuator pairs, $l_0 = l_{max}$ is the rest length of REBO, r_p is the radius of the pulley and $\theta_{m,i}$ is the angle of rotation of the corresponding motor.

The position vector of the center of the top triangle is \mathbf{p}_c . For this three DOF system, the orientation of the top triangle is coupled with its position, which can be fully described with $q_{tt} = (r, \theta, \phi) \in [l_{min}, l_{max}] \times \mathbb{S}^1 \times \mathbb{S}^1 = Q_{tt}$, where r is the length of \mathbf{p}_c , θ is the angle between \mathbf{p}_c and the x axis, and

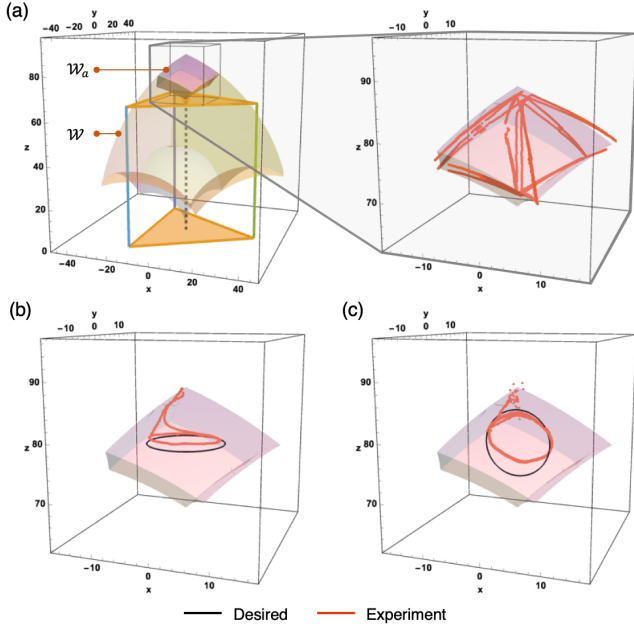


Fig. 5. (a) The kinematically achievable workspace \mathcal{W} and the actuator achievable workspace \mathcal{W}_a of the Juggler's top plate. The bent cuboid is the simulation where the red line is the experimental trajectories of the envelope of the workspace. (b) horizontal circle test (c) vertical circle test.

ϕ is the angle between \mathbf{p}_c and the y axis. The kinematics $q_{tt} = f_2(q_{la})$ can be found by observing the geometry of the model to be

$$r = \frac{1}{3}(l_1 + l_2 + l_3) \quad (1)$$

$$\theta = \cos^{-1} \left(\frac{1}{6d}(-2l_1 + l_2 + l_3) \right) \quad (2)$$

$$\phi = \cos^{-1} \left(\frac{1}{2\sqrt{3}d}(-l_2 + l_3) \right). \quad (3)$$

The position vector $\mathbf{p}_c = [x_c \ y_c \ z_c]^T \in \mathbb{R}^3$ can be described in Cartesian coordinates as

$$\begin{aligned} \mathbf{p}_c &= f_{cc}(q_{tt}) \\ &:= [r \cos \theta \ r \cos \phi \ r\sqrt{1 - \cos^2 \theta - \cos^2 \phi}]^T. \end{aligned} \quad (4)$$

Unlike a Delta parallel machine, the orientation of the top plate varies with respect to the position of the top plate, and the unit normal vector of the top plate can be written as $\mathbf{n}_{\text{top}} = [\sin 2\theta \ \sin 2\phi \ \sqrt{1 - \sin^2 2\theta - \sin^2 2\phi}]^T$. When controlling the robot, the input command to the motor can be found by the inverse map of the kinematics as

$$q_m = g_{ik}(\mathbf{p}_c) = f_1^{-1} \circ f_2^{-1} \circ f_{cc}^{-1}(\mathbf{p}_c). \quad (5)$$

IV. KINEMATIC TASK: POINTING

The trajectory of the REBO Juggler's top plate can be planned within its constrained workspace, and the controlling command of the motor can be found through the inverse map g_{ik} . The kinematically achievable workspace of the top plate is the image through the kinematic model of the extreme of the length of the tendon l_{max} and l_{min} and can be described as $\mathcal{W} = \{\mathbf{p}_c | \mathbf{p}_c = f_{cc} \circ f_2(q_{la}), q_{la} \in Q_{la}\}$. The actuator achievable workspace \mathcal{W}_a is a subset of the full workspace \mathcal{W} , and is limited by the continuous torque τ_c of the motor, where its minimum value can be found as $l_{min} = l_{max} - (\tau_c/r_p)/K_s$,

where K_s is the effective stiffness of one REBO. Since this research explores the structure with high stiffness, the achieved compression $= l_{max} - l_{min}$ is small. Fig. 5 shows the image through the kinematic model \mathcal{W} , with $l_{max} = 88$ mm and $l_{min} = 66$ mm. The constrained workspace \mathcal{W}_a has a volume of 4980.95 mm^3 .

To demonstrate the mobility of the top plate, we tracked the position of the top plate under varying control inputs using an OptiTrack motion capture system. The first experiment was an open-loop workspace boundary test. The boundary of the workspace occurs where at least one of the linear actuators is at its maximum (minimum) length and the others change length. We measured the trajectory of the top plate when the linear actuators were moved between l_{min} and l_{max} while holding at least one other constant. The experimental results are shown as the red trajectories in Fig. 5(a), which capture the structure of the simulated workspace, and has a 14.4% rms error from the predicted boundary. The volume of the convex hull of these trajectories is 5426.26 mm^3 , which has a 8.94% error from the predicted volume.

To check the accuracy of the kinematic model, we commanded the top plate to follow circular trajectories that were generated to lie within the workspace. The top plate was set to follow first a horizontal circle with radius 7 mm, then a vertical circle with radius 6 mm, both centered at $[0 \ 0 \ \frac{1}{2}(l_{min} + l_{max})]^T$. Fig. 5(b) and 5(c) show the results of the two experiments. The rms errors for the two tracking tests were 11.32% and 14.66%, respectively. Fig. 5(c) shows that the real and desired trajectories of the vertical circle deviate closer to the bottom. This is because the actuator needs more torque for greater compression, yet is limited by the motors' maximum continuous torque. This limitation is expected to be improved when we reduce the diameter of the pulley, allowing the actuator to transmit more compressive force to the linear REBO spring.

V. DYNAMICAL TASK: VERTICAL JUGGLING

Reflecting the past traditions of the field of dynamical locomotion, the core problem of stable running [36] can be reduced to the problem of stable vertical hopping [37], for which a purely vertical juggle is a representative surrogate [38], [39]. Thus, as a proof-of-concept task, the REBO juggler's ball, its dynamical "environment," is restricted to purely vertical motion by confinement within a tube mounted on the paddle, while the parallel three REBO elements can be viewed as an actively loaded single vertical spring. Since the REBO exhibits elastic hysteresis, the total energy of the ball would be substantially diminished by each encounter with a relaxed paddle, hence additional energy must be pre-loaded into the waiting spring so as to impart at each hit the work needed to keep the ball bouncing. Specifically, to pump energy into the coupled robot-environment system, the motors work on the REBO by pre-compressing it to a fixed position \mathbf{p}_{c_p} , before the ball lands on the paddle. When the pad detects contact, the REBO then releases the energy into the ball by resetting the set point of the tendon to its rest length \mathbf{p}_{c_r} . Fig. 6(a) shows a successful juggling period of one of the open-loop experiments presented in this section.

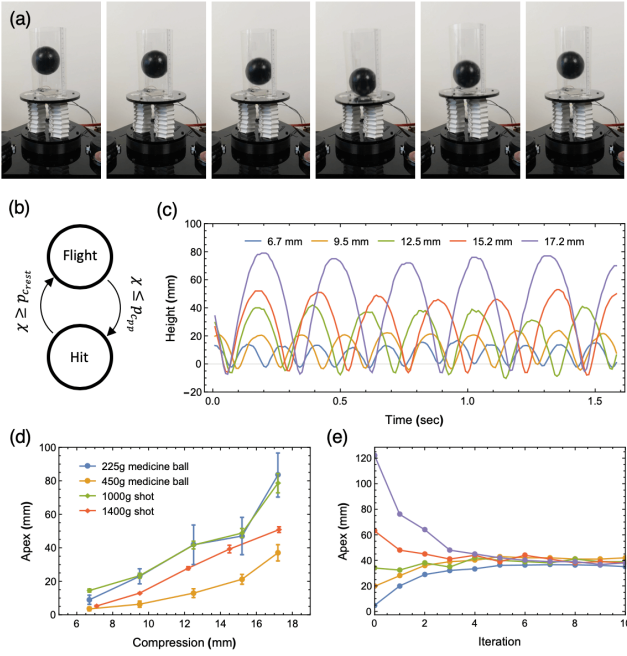


Fig. 6. Vertical juggling (a) Snapshot of the experiment with an interval of 1/30 sec. (b) State machine of the juggling task. (c) Trajectory of the 1 kg shot under different pre-pressed REBO conditions. (d) Pre-pressed length of REBO v.s. juggling height of several different balls with STDs. (e) Transient responses (apex vs. iteration) of the 1 kg shot from a variety of initial heights, exhibiting the asymptotically stable fixed point at 4 cm associated with the 12.5 mm pre-compression setting plotted in (d).

Juggling arises from a hybrid dynamical system comprising two modes: “Flight” and “Hit”, as shown in Fig. 6(b). In the “Flight” mode, the launched ball exhibits a ballistic trajectory governed by the lossless constant gravity system $m_b \ddot{\chi} = -m_b g$, where m_b and χ are the mass and the position of the ball, respectively. After the ball’s launch, the juggler quickly resets back to its pre-compressed position. Because the compliant REBO structure has a mass that is negligible (less by at least an order of magnitude) relative to that of the frame or ball, we ignore any REBO dynamics and treat the reset as instantaneous. The “Flight” mode stops when the force sensor on the paddle is triggered by the ball’s contact and the system enters the “Hit” mode. Now, the ball rides down the paddle of the compressing REBO structure, and the whole system can be considered as a mass on a spring. The REBO elastic energy is imparted to the ball’s mass as governed by the dynamics $m_b \ddot{\chi} = -K_{es}(\chi - r_{rest}) - B_s \dot{\chi} - m_b g$, where $K_{es} = 3K_s$ is the juggler’s effective stiffness and B_s its damping coefficient. The “Hit” mode ends when the REBO reaches its rest length, whereupon the ball lifts off as reported by the force sensor, the motor re-engages the tendon, and the system re-enters the “Flight” mode.

REBO’s Hookean force-extension curve (Fig. 2(c)) implies that the more it is compressed, the more energy it stores; hence, because it can sustain high forces under load, the juggler injects more energy into the ball in “Hit” mode with greater pre-compression, resulting in higher apex positions. Fig. 6(c) documents this increase in vertical amplitude for a 1 kg shot under increasing commanded pre-compression lengths $\mathbf{p}_{com} = \mathbf{p}_{cr} - \mathbf{p}_{cp}$. A slow motion video of 120

fps has been filmed for every trial and the trajectory of the ball was found using “Tracker” (<https://physlets.org/tracker/>). The result confirms that the more REBO is pre-compressed, the higher the ball can be juggled.

Fig. 6(d) summarizes the results of repeated (100 juggling cycles each) experiments with several different balls being juggled under different pre-compressed lengths by plotting the mean and standard deviation of measured apex heights. Two shots of mass 1 kg and 1.4 kg were selected because their resilient rigid metal composition yields an approximately elastic collision, presenting a “lossless environment” to the juggler. In contrast, two sand-loaded medicine balls of mass 225 g and 450 g yield highly inelastic collisions chosen to confront the juggler with a “highly dissipative environment.” It is clear that the average apex height is monotonically increasing with respect to the pre-compression for all the balls. For the same compressive pre-load condition, the heavier balls have a lower apex than the lighter ones as expected if each pair is restored to the same steady energy state. Here, since the medicine balls dissipate more stored energy than the shots, making them harder to juggle, the juggler lofts the 225 g ball to roughly the same steady state apex as the 1000 g shot. We can summarize the energetic properties of the REBO structure with respect to its work on the balls as follows. The energy loaded into the REBO structure by the DC servos’ pre-compression work is $E = \frac{1}{2} K_{es} |\mathbf{p}_{com}|^2 = \frac{1}{2} (3105) * (0.0172)^2 \approx 0.5 \text{ J}$ for the 1 kg shot bounced at a height of 8 cm. Since the “Hit” mode has a typical duration of 0.02 s the REBO delivers a mechanical power output of 25 W.

Fig. 6(e) plots the trajectories over the course of the first ten successive collisions (out of hundreds recorded) with the juggler’s paddle of the apex heights of the 1 kg shot starting from five different initial conditions, all subject to the same pre-compressed REBO length of 12.5 mm. Treating the apex height as the coordinate chart for the Poincaré section of this hybrid dynamical system, the plot demonstrates the asymptotic stability of the period one hybrid limit cycle by displaying convergence to the 4 cm fixed point of the associated Poincaré (or “return”) map [38]. The results suggest the relatively large basin of attraction (set of initial heights that are successfully juggled up or down to the desired 4 cm steady state apex height) achieved by the juggler consistent with a high power actuator along the lines discussed in [39].

VI. DISCUSSION AND FUTURE WORK

The resilient, programmable stiffness of the lightweight, deformable REBO structure allows us to transfer energy through the 1 kg shot at roughly 25 W, repeatedly over the course of thousands of hits with very little fatigue, as attested by the highly repeatable asymptotically stable steady state juggling cycles, lofting the 1 kg load to nearly 10 cm heights. Thus, our soft REBO breaks new ground in the literature by transducing energy¹ of about $(25 \text{ W}) / (0.22 \text{ kg}) \approx 110 \text{ (W/kg)}$, which,

¹The closest comparable analysis of mass-specific power in the soft robotics literature reports a fluid vacuum actuator’s 2 kW/kg tensile work rate [19]. In contrast, we measure a passive meta-material’s capacity to recruit energy loaded in its mechanical structure to push the ball away (at the 110 W/kg specific power rate).

when distributed across the repeating origami structure, is sufficient to power the task of vertical juggling — an established route to dynamical dexterity in conventional robotics [38]. Furthermore, since the stiffness of REBO changes by up to an order of magnitude solely by changing the geometric parameters, the mechanical output power can be adjusted to suit diverse applications, notwithstanding the reliance on a single monolithic material across all the varying designs. Indeed, we have begun work to turn the REBO juggler “upside down,” aiming for a power autonomous “soft” hopper capable of lifting its batteries and actuators to comparable apex states. The experiments presented here focus on merely modifying the cone angle β for REBOs made of the same materials with the same thicknesses and having the same number of sides and side lengths. Future work yielding a more formal understanding of the REBO’s mechanical properties will afford a generalizable scaling law to achieve programmable compliance for a broad range of robotics applications. We are currently working on tuning the stiffness of the material on the fly, making an adaptive robot limb for various tasks, which will be reported in future work.

REFERENCES

- [1] M. Buehler and D. E. Koditschek, “Robotics in an intermittent dynamical environment: A prelude to juggling,” in *Proc. 26th IEEE Conference on Decision and Control*, Dec 1987. [Online]. Available: https://kodlab.seas.upenn.edu/uploads/Kod/BuehlerKoditschek87prelude_juggling.pdf
- [2] M. Buehler and D. Koditschek, “Analysis of a simplified hopping robot,” in *1988 IEEE International Conference on Robotics and Automation, 1988. Proceedings*, Apr 1988, pp. 817–819 vol.2.
- [3] R. R. Burridge, A. A. Rizzi, and D. E. Koditschek, “Toward a systems theory for the composition of dynamically dexterous robot behaviors,” in *ROBOTICS RESEARCH-INTERNATIONAL SYMPOSIUM-*, vol. 7, 1996, pp. 149–161.
- [4] A. Rizzi and D. Koditschek, “An active visual estimator for dexterous manipulation,” *Robotics and Automation, IEEE Transactions on*, vol. 12, no. 5, pp. 697–713, 1996.
- [5] M. Venkadesan, J. Guckenheimer, and F. J. Valero-Cuevas, “Manipulating the edge of instability,” *Journal of Biomechanics*, vol. 40, no. 8, pp. 1653–1661, Jan 2007.
- [6] E. L. Lawrence, I. Fassola, I. Werner, C. Leclercq, and F. J. Valero-Cuevas, “Quantification of dexterity as the dynamical regulation of instabilities: Comparisons across gender, age, and disease,” *Frontiers in Neurology*, vol. 5, 2014.
- [7] F. J. Valero-Cuevas, N. Smaby, M. Venkadesan, M. Peterson, and T. Wright, “The strength-dexterity test as a measure of dynamic pinch performance,” *Journal of Biomechanics*, vol. 36, no. 2, pp. 265–270, Feb 2003.
- [8] S. Revzen and D. E. Koditschek, “Why we need more degrees of freedom,” *Procedia IUTAM*, vol. 20, pp. 89–93, 2017.
- [9] I. W. Hunter, J. M. Hollerbach, and J. Ballantyne, “A comparative analysis of actuator technologies for robotics,” *Robotics Review*, vol. 2, pp. 299–342, 1992.
- [10] C. Laschi and M. Cianchetti, “Soft robotics: new perspectives for robot bodyware and control,” *Frontiers in bioengineering and biotechnology*, vol. 2, p. 3, 2014.
- [11] L. L. Howell, *Compliant mechanisms*. John Wiley & Sons, 2001.
- [12] A. D. Marchese, C. D. Onal, and D. Rus, “Autonomous soft robotic fish capable of escape maneuvers using fluidic elastomer actuators,” *Soft Robotics*, vol. 1, no. 1, pp. 75–87, 2014.
- [13] M. T. Tolley, R. F. Shepherd, M. Karpelson, N. W. Bartlett, K. C. Galloway, M. Wehner, R. Nunes, G. M. Whitesides, and R. J. Wood, “An untethered jumping soft robot,” in *2014 IEEE/RSJ International Conference on Intelligent Robots and Systems*. IEEE, 2014, pp. 561–566.
- [14] C. D. Onal, R. J. Wood, and D. Rus, “An origami-inspired approach to worm robots,” *IEEE/ASME Transactions on Mechatronics*, vol. 18, no. 2, pp. 430–438, April 2013.
- [15] S. Li, J. J. Stampfli, H. J. Xu, E. Malkin, E. V. Diaz, D. Rus, and R. J. Wood, “A vacuum-driven origami “magic-ball” soft gripper,” in *2019 International Conference on Robotics and Automation (ICRA)*, May 2019, pp. 7401–7408.
- [16] A. M. Hoover, E. Steltz, and R. S. Fearing, “RoACH: An autonomous 2.4 g crawling hexapod robot,” in *2008 IEEE/RSJ International Conference on Intelligent Robots and Systems*, 2008, pp. 26–33.
- [17] J. P. Whitney, P. S. Sreetharan, K. Y. Ma, and R. J. Wood, “Pop-up book MEMS,” *Journal of Micromechanics and Microengineering*, vol. 21, no. 11, p. 115021, 2011.
- [18] S.-J. Kim, D.-Y. Lee, G.-P. Jung, and K.-J. Cho, “An origami-inspired, self-locking robotic arm that can be folded flat,” *Science Robotics*, vol. 3, no. 16, p. eaar2915, 2018.
- [19] S. Li, D. M. Vogt, D. Rus, and R. J. Wood, “Fluid-driven origami-inspired artificial muscles,” *Proceedings of the National Academy of Sciences*, vol. 114, no. 50, pp. 13 132–13 137, 2017.
- [20] R. V. Martinez, C. R. Fish, X. Chen, and G. M. Whitesides, “Elastomeric origami: programmable paper-elastomer composites as pneumatic actuators,” *Advanced functional materials*, vol. 22, no. 7, pp. 1376–1384, 2012.
- [21] K. Zhang, C. Qiu, and J. S. Dai, “An extensible continuum robot with integrated origami parallel modules,” *Journal of Mechanisms and Robotics*, vol. 8, no. 3, p. 031010, 2016.
- [22] J. Santoso, E. H. Skorina, M. Luo, R. Yan, and C. D. Onal, “Design and analysis of an origami continuum manipulation module with torsional strength,” in *2017 IEEE/RSJ International Conference on Intelligent Robots and Systems (IROS)*, Sep. 2017, pp. 2098–2104.
- [23] D. M. Sussman, Y. Cho, T. Castle, X. Gong, E. Jung, S. Yang, and R. D. Kamien, “Algorithmic lattice kirigami: A route to pluripotent materials,” *Proceedings of the National Academy of Sciences*, vol. 112, no. 24, pp. 7449–7453, 2015.
- [24] Y. Tang, G. Lin, S. Yang, Y. K. Yi, R. D. Kamien, and J. Yin, “Programmable kiri-kirigami metamaterials,” *Advanced Materials*, vol. 29, no. 10, p. 1604262, 2017.
- [25] A. Johnson and D. Koditschek, “Legged self-manipulation,” *IEEE Access*, vol. 1, pp. 310–334, 2013.
- [26] H. Yuan, J. H. Pikul, and C. Sung, “Programmable 3-d surfaces using origami tessellations,” in *7th International Meeting on Origami in Science, Mathematics, and Education*, 2018, pp. 893–906.
- [27] J. A. Faber, A. F. Arrieta, and A. R. Studart, “Bioinspired spring origami,” *Science*, vol. 359, no. 6382, pp. 1386–1391, 2018.
- [28] S. Mintchev, J. Shintake, and D. Floreano, “Bioinspired dual-stiffness origami,” *Science Robotics*, vol. 3, no. 20, p. eaau0275, 2018.
- [29] A. Reid, F. Lechenault, S. Rica, and M. Adda-Bedia, “Geometry and design of origami bellows with tunable response,” *Physical Review E*, vol. 95, no. 1, p. 013002, 2017.
- [30] E. T. Filipov, T. Tachi, and G. H. Paulino, “Origami tubes assembled into stiff, yet reconfigurable structures and metamaterials,” *Proceedings of the National Academy of Sciences*, vol. 112, no. 40, pp. 12 321–12 326, 2015.
- [31] N. P. Bende, T. Yu, N. A. Corbin, M. A. Dias, C. D. Santangelo, J. A. Hanna, and R. C. Hayward, “Overcurvature induced multistability of linked conical frusta: how a ‘bendy straw’ holds its shape,” *Soft matter*, vol. 14, no. 42, pp. 8636–8642, 2018.
- [32] J. Carlson, J. Friedman, C. Kim, and C. Sung, “REBOund: Untethered origami jumping robot with controllable jump height,” in *IEEE International Conference on Robotics and Automation*, 2020.
- [33] C. Qiu, V. Aminzadeh, and J. S. Dai, “Kinematic analysis and stiffness validation of origami cartons,” *Journal of Mechanical Design*, vol. 135, no. 11, p. 111004, 2013.
- [34] K. C. Galloway, J. E. Clark, and D. E. Koditschek, “Design of a multi-directional variable stiffness leg for dynamic running,” in *ASME 2007 International Mechanical Engineering Congress and Exposition*. American Society of Mechanical Engineers, 2007, pp. 73–80.
- [35] “Ghost Robotics,” <https://www.ghostrobotics.io>.
- [36] M. H. Raibert, *Legged robots that balance*. MIT press, 1986.
- [37] —, “Dynamic stability and resonance in a legged hopping machine,” in *Conference on Theory and Practice of Robots and Manipulators, IFToMM*, 1983, pp. 352–367.
- [38] M. Buehler, D. E. Koditschek, and P. Kindlmann, “A simple juggling robot: Theory and experimentation,” in *Experimental Robotics I*. Springer, 1990, pp. 35–73.
- [39] D. E. Koditschek and M. Buehler, “Analysis of a simplified hopping robot,” *The International Journal of Robotics Research*, vol. 10, no. 6, pp. 587–605, 1991.